

Nanoconfinement promotes CO₂ electroreduction to methanol on a molecular catalyst

Received: 13 November 2024

Accepted: 28 July 2025

Published online: 09 August 2025

Check for updates

Guoshuai Shi^{1,3}, Wendi Zhang^{2,3}, Yikun Kang^{1,3}, Jin Zhao¹, Tingyu Lu¹, Chunlei Yang¹, Mingwei Chang¹, Yuluo Shen¹, Xinyang Gao¹, Jing Wu¹, Ye-Fei Li¹✉, Kecheng Cao²✉ & Liming Zhang¹✉

Confining catalysis within a nanospace can effectively regulate intermediate configurations and product distributions. Here, we demonstrate the inner cavity of carbon nanotubes (CNTs) as a nanoreactor to promote the electrochemical conversion of CO₂ to methanol (CH₃OH). Cobalt phthalocyanine (CoPc) molecules are rationally incorporated into CNTs of varying diameters, exhibiting different CH₃OH selectivities. CoPc confined within the CNTs is more prone to CH₃OH production, whereas CoPc located on the exterior primarily facilitates CO formation. Operando spectroelectrochemical measurements and theoretical calculations demonstrate that the nanoconfined environment effectively accumulates CO as an intermediate, introduces structural deformation in CoPc molecules, enhances *CO adsorption on Co sites, and consequently improves CH₃OH production. This work underscores the significance of local microenvironment in electrocatalysis and presents an approach to enhancing deep-reduction product selectivity in molecular catalysts through nanoconfinement.

Confining catalysis within a nanospace offers a compelling strategy to regulate catalytic specificity. As demonstrated in thermal catalysis within well-defined nanocavities, certain reaction pathways can be selectively promoted or inhibited due to spatial constraints, modulation of adsorbate configurations, and interactions between intermediates and the cavity interior^{1–3}. Consequently, significant alterations in product distributions have been observed in various catalytic processes, including syngas conversion^{4,5}, CO oxidation^{6,7}, propane dehydrogenation^{8,9}, and stereoselective cyanosilylation¹⁰, upon confinement within nanospaces. Beyond thermocatalysis, the nanoconfinement effect has also been identified in electrocatalysis, particularly in complex conversion processes involving multiple intermediates, where their adsorption can be significantly modulated in a confined space^{11–15}. For instance, electrochemical CO₂ conversion

to valuable carbon-based fuels involves intricate electron-proton transfer pathways, generating a diverse range of carbon intermediates¹⁶. Therefore, modulating the interactions between intermediates and catalytic centers in a nanoconfined environment is expected to provide significant opportunities for tailoring the final product distribution in CO₂ electroreduction.

In electrochemical CO₂ reduction (CO₂R), selectively converting CO₂ into high-value-added and deeply reduced liquid-phase product remains a significant challenge and an active research focus. To date, the most studied metal for effectively transforming CO₂ into deeply reduced chemicals is copper (Cu)^{17–19}. However, Cu exhibits poor selectivity towards multiple fuel products, thereby increasing the complexity of downstream product separation. This poor selectivity stems from the high structural sensitivity of CO₂ transformation on

¹Department of Chemistry, State Key Laboratory of Porous Materials for Separation and Conversion, iChEM (Collaborative Innovation Center of Chemistry for Energy Materials), Shanghai Key Laboratory of Molecular Catalysis and Innovative Materials, Fudan University, Shanghai, China. ²School of Physical Science and Technology & Shanghai Key Laboratory of High-resolution Electron Microscopy, Shanghai Tech University, Shanghai, China. ³These authors contributed equally: Guoshuai Shi, Wendi Zhang, Yikun Kang. ✉e-mail: yefeili@fudan.edu.cn; caokch@shanghaitech.edu.cn; zhanglm@fudan.edu.cn

heterogeneous Cu surfaces^{18–20}. As an alternative to metallic catalysts, molecular catalysts such as metal complexes feature single-atomic site configurations with well-defined M-N₄ coordination environments, serving as ideal platforms for mechanistic investigations^{21,22}. However, this class of catalysts rarely achieves deeply reduced products beyond CO^{21–26}, as *CO (adsorbed CO intermediate) desorption is highly favored at these single-atomic centers. Recently, several studies have reported the electrochemical production of methanol (CH₃OH) from CO₂ at the single-Co site of cobalt phthalocyanine (CoPc)^{27,28}, particularly when CoPc is dispersed on carbon nanotubes (CNTs). While the mechanistic aspects of CH₃OH formation have been explored^{27–32}, atomic-level insights into the precise structure of CoPc/CNTs and the influence of structural modifications on CO₂R pathway selection remain elusive.

CNTs feature well-defined one-dimensional hollow interiors enclosed by curved graphene walls, offering significant potential for the encapsulation of molecules or nanoparticles within their nanocavity^{33–39}. Catalysts confined within such nanoscale environments may behave differently compared to their bulk counterparts. Typically, CoPc catalyzes the electrochemical reduction of CO₂ to CO rather than >2e⁻ products^{22,25,26}, requiring more than two electrons per molecules for product formation. This selectivity arises from the weak adsorption and short residence time of *CO on Co catalytic sites. However, this behavior can be significantly modified within a nanoconfined space, such as the interior of a CNT. In such a confined environment, the residence time of desorbed CO molecules is inevitably extended due to steric constraints, leading to CO accumulation within the confined space and restricting *CO desorption, in accordance with reaction equilibrium principles. Since *CO serves as a key intermediate for the formation of deeply reduced products, we hypothesize that this phenomenon may facilitate the further reduction of *CO to >2e⁻ products, such as CH₃OH, as schematically illustrated in Fig. 1.

In this study, we systematically designed CNTs with five different diameters as scaffolds to encapsulate CoPc, revealing a strong correlation between CH₃OH yield and the inner diameter (ID) of CNTs. Notably, CH₃OH selectivity was significantly enhanced when CoPc was confined within CNTs of optimal ID. Moreover, modifications in the CO₂ supply pathway at the exterior of CNTs were found to have a negligible impact on CH₃OH production inside. Operando spectroelectrochemical characterizations and density functional theory (DFT) calculations demonstrated the confined space effectively enriched CO and induced structural deformation in CoPc molecules, thereby substantially improving *CO adsorption on Co sites and facilitating its further reduction to CH₃OH. This work highlights the critical influence of local electrochemical microenvironments and establishes nanoconfinement as a viable strategy to promote deep-reduced product formation in CO₂ electrolysis using molecular catalysts.

Results

Encapsulating CoPc in CNTs

Since the ID of CNT dictates molecular encapsulation, we investigated CNTs with five different diameters as scaffolds for embedding CoPc, denoted as CNTs(I, II, III, IV, and V), with increasing ID (see Methods for details). The IDs and outer diameters (ODs) of CNTs(I–V) were determined based on high-resolution transmission electron microscopy (HR-TEM) observations and summarized in Supplementary Table 1. According to previous studies, CNTs are expected to be wettable by liquids with a surface tension below 100–200 mN m⁻¹, allowing for their filling through the open ends^{36,39}. A schematic representation of the catalyst design is shown in Fig. 2a.

To confirm the location of CoPc within different CNTs, we employed HR-TEM imaging and corresponding TEM simulations. Notably, CoPc was exclusively observed on the exterior surface of CNT(I), as its ID (1–2 nm) is comparable to the molecular size of CoPc (~1.2 nm), restricting capillary-driven encapsulation (Fig. 2b). Structural models and TEM simulations further demonstrated that CoPc molecules wrapped around CNT(I) rather than being incorporated inside. In contrast, CoPc exhibited a high probability of being encapsulated within CNTs(II–V), which possess larger IDs (Fig. 2c and Supplementary Fig. 1). Aberration-corrected high-angle annular dark-field scanning transmission electron microscopy (HAADF-STEM) further confirmed the spatial distribution of Co within CNTs (Fig. 2d). The presence of high-density bright spots corresponding to single Co sites predominantly inside CNTs suggests the successful encapsulation of CoPc molecules. The precise Co content was quantified via inductively coupled plasma optical emission spectrometry (ICP-OES), revealing that CoPc/CNTs(I–V) exhibited comparable Co loadings (Supplementary Table 2).

Promoted CH₃OH production at the interior of CNTs

We evaluated the catalytic activity and selectivity of CoPc/CNTs(I–V) in a CO₂-saturated 0.1 M KHCO₃ aqueous solution (pH = 6.8 ± 0.1) using a two-compartment H-cell at room temperature (23 ± 2 °C). Notably, despite having similar CoPc loading concentrations, CoPc/CNTs(I–V) exhibited significant variations in CH₃OH selectivity depending on their IDs. For CoPc/CNT(I), where most CoPc molecules were located on the exterior surface of CNTs, CO and H₂ were observed as the predominate products (Fig. 3a). The maximum Faradaic efficiency (FE) for CH₃OH was below 3% at –0.96 V versus the reversible hydrogen electrode (V_{RHE}). In contrast, CoPc/CNTs(II–V) effectively catalyzed CO₂ reduction to CH₃OH, as illustrated in Fig. 3b and Supplementary Fig. 2. In particular, CoPc/CNT(III) exhibited a strong preference for CH₃OH production, achieving a maximum FE of approximately 41% and a partial current density of 7.3 mA/cm² at –0.96 V_{RHE} (Fig. 3c). Given the HR-TEM observations, it is reasonable to infer that CoPc molecules encapsulated within CNTs provide active sites for CH₃OH formation. The turnover frequency (TOF) was calculated based on both the CH₃OH production rate (Supplementary Fig. 3) and the

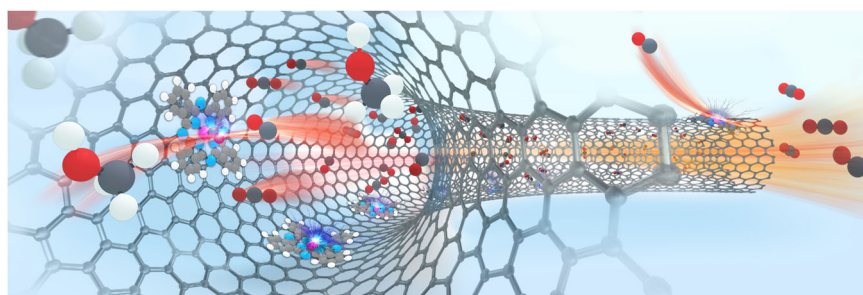


Fig. 1 | A schematic illustration depicting the inner cavity of a CNT as a nanoreactor for promoting CO₂-to-CH₃OH conversion.

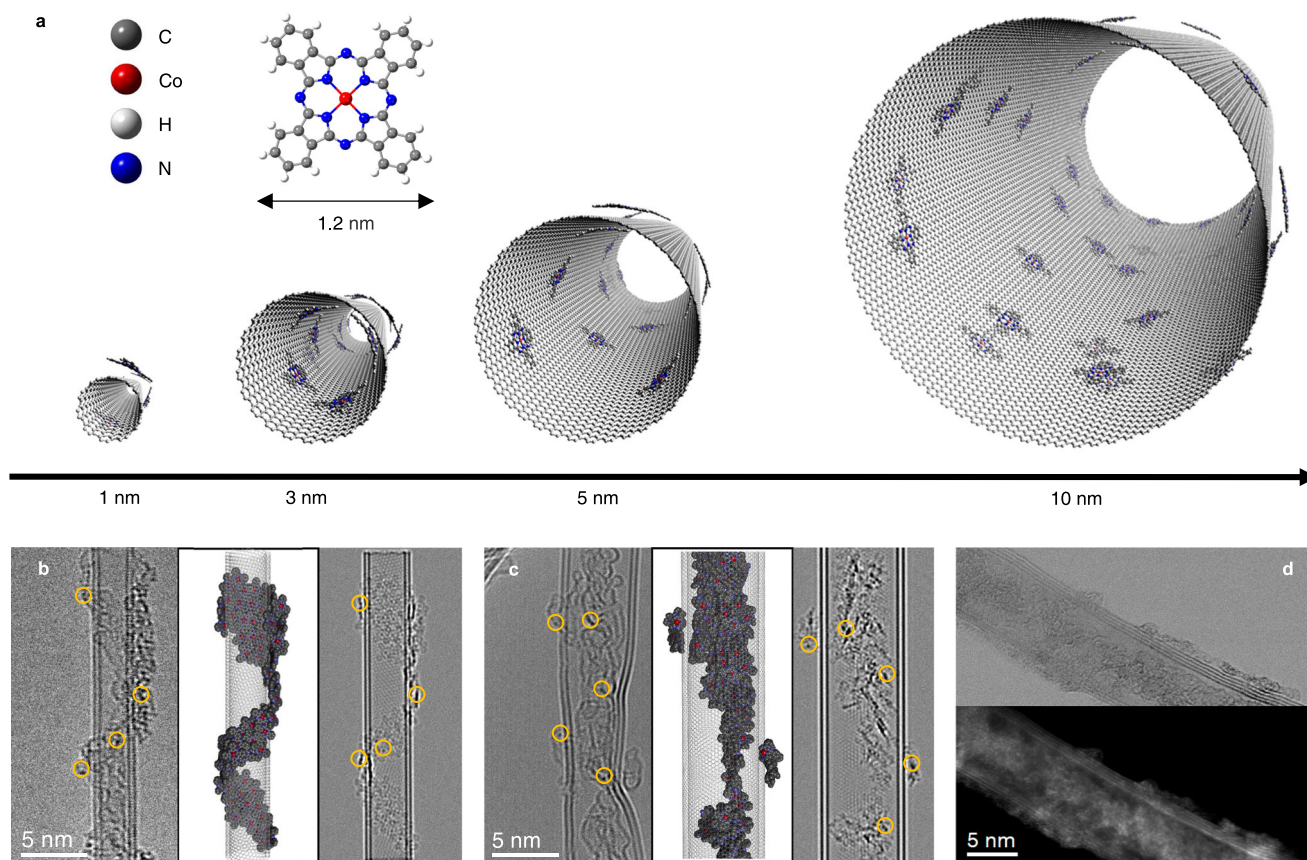


Fig. 2 | Encapsulation of CoPc within CNTs. **a** Schematic illustration depicting the encapsulation of CoPc inside CNTs with varying IDs. The inset presents the molecular structure of CoPc. **b, c**, HR-TEM images (left) of CoPc/CNT(I) (**b**) and CoPc/CNT(III) (**c**), accompanied by corresponding structural models (middle) and

simulated TEM images (right). The regions with darker contrast, attributed to Co atoms, are highlighted with yellow circles. **d** HR-TEM (top) and HADDF-STEM (bottom) images of CoPc/CNT(III) at the same location, confirming the successful encapsulation of CoPc molecules.

number of Co atoms in CoPc/CNTs(I-V). As illustrated in Supplementary Fig. 4, the TOF values of CoPc/CNTs(II-V) exhibit a significant enhancement, approximately one order of magnitude higher than that of CoPc/CNT(I). This pronounced difference underscores the critical role of nanoconfinement in promoting CH_3OH production.

To confirm that encapsulated CoPc molecules exhibit higher activity toward CH_3OH production, we modulated the relative CO_2 concentrations inside and outside CNTs. Due to mass transport limitations within CNTs, the CO_2 concentration in the interior is less sensitive to external CO_2 supply variations than that in the exterior. CO_2R was performed using CoPc/CNT(III) in a flow cell with a gas-diffusion electrode (GDE), a setup widely employed to enhance CO_2 supply. Unlike the product distribution observed in the H-cell, CO was the predominant product at all tested potentials in the flow cell (Fig. 3d and Supplementary Fig. 5). This drastic enhancement in CO production can be attributed to the increased CO_2 availability at the exterior surface of CNTs, where CoPc predominantly catalyzes CO_2 reduction to CO. However, due to mass transport constraints, the CO_2 concentration inside CNTs remained largely unchanged, explaining the suppressed CH_3OH formation in the flow cell. These findings further support that encapsulated CoPc molecules preferentially catalyze CO_2 reduction to CH_3OH . To further validate our hypothesis, we reduced the CO_2 concentration in the H-cell by diluting CO_2 with Ar and performed CO_2R on CoPc/CNT(III). Under a 10 vol.% CO_2 condition, CO_2R was significantly inhibited, and hydrogen evolution became the dominant reaction

(Supplementary Fig. 6). Interestingly, compared with the 100 vol.% CO_2 condition, the FE of CO sharply decreased from 20 to 5% at $-0.95 \text{ V}_{\text{RHE}}$, whereas the FE of CH_3OH only declined from 41 to 29%. We attribute this difference in selectivity to the distinct CO_2 concentration variations inside and outside CNTs when CO_2 supply was diluted. The CO_2 concentration inside CNTs was less affected by external dilution due to inherent mass diffusion limitations, leading to relatively stable CH_3OH production. In summary, these results demonstrate that CO and CH_3OH are primarily produced by CoPc molecules located on the exterior and interior surfaces of CNTs, respectively.

To further confirm the preferential CO selectivity of CoPc located on the external surface of CNTs, we investigated the influence of synthesis conditions on the CO_2R selectivity of CoPc/CNT(III). By omitting ultrasonication and shortening the stirring duration (see Methods), we reduced the likelihood of CoPc molecules penetrating into the interior of CNT(III), which resulted in decreased CH_3OH selectivity and increased CO selectivity (Supplementary Fig. 7a, c). Furthermore, we found that the incorporation of CoPc into CNTs primarily occurs during the solvent-wetting step, while undissolved CoPc tends to remain on the outer surface. Consequently, reduced CoPc solubility in the organic solvent leads to fewer CoPc molecules being encapsulated within the CNT interior. To further suppress CoPc encapsulation, ethanol was employed as the solvent (see Methods), owing to its significantly lower CoPc solubility compared to N,N-dimethylformamide (DMF)⁴⁰. As shown in Supplementary Fig. 7b, c, CoPc/CNT(III) synthesized in ethanol exhibited significantly lower

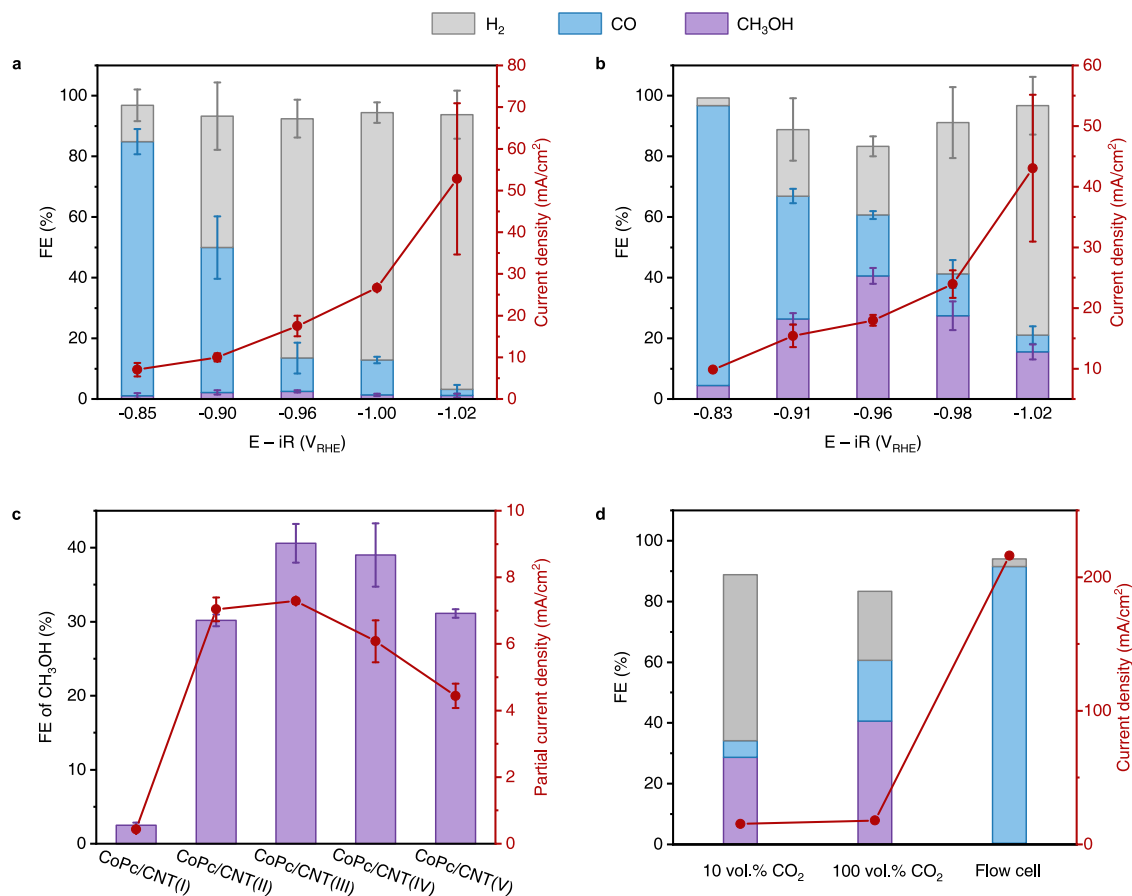


Fig. 3 | Enhanced CH₃OH production within the CNTs interior. **a–b** Product distribution and corresponding current density of CO₂R in 0.1 M CO₂-saturated KHCO₃ solution (pH = 6.8 ± 0.1) at various applied potentials for CoPc/CNT(I) (**a**) and CoPc/CNT(III) (**b**), respectively. **c** Comparison of maximum FE and partial current density of CH₃OH among CoPc/CNTs(I–V). Data are presented as mean values ± standard deviation. The standard deviation is obtained based on three

independent samples. **d** Comparative analysis of current density and FE of CH₃OH in a flow cell versus an H-cell, under 100 vol.% and 10 vol.% CO₂ supply conditions. The resistance value of H-cell and flow cell is 10 ± 2 Ω and 2.2 ± 0.3 Ω, respectively. The gas flow rate of H-cell and flow cell is 5 mL/min and 20 mL/min, respectively. The mass loading is -0.4 mg/cm_{geo}². All measurements were performed at room temperature (23 ± 2 °C).

CH₃OH selectivity and higher CO selectivity than its DMF-synthesized counterpart. These findings provide strong evidence that CoPc molecules located on the CNT exterior preferentially promote CO₂ reduction to CO rather than CH₃OH.

Enriched CO and structural deformation of CoPc under nanoconfinement

To rationalize the high CH₃OH yield observed at the CNT interior, we first propose that the localized CO enrichment within the confined space plays a crucial role in CH₃OH production. The steric confinement imposed by the carbon nanowalls leads to a higher CO concentration around CoPc, thereby restricting the free desorption of *CO from Co sites and facilitating its further reduction. To validate this hypothesis, we performed electrochemical CO reduction (COR) in a flow cell equipped with a GDE. Compared to CO₂R, COR significantly enhanced both the selectivity and yield of CH₃OH. The maximum FE and partial current density on CoPc/CNT(III) reached 74% and 20.1 mA/cm² at -0.94 V_{RHE}, respectively (Supplementary Fig. 8a). These results underscore the essential role of high local CO concentration in CH₃OH production. Additionally, the COR performance of CoPc/CNT(I) was evaluated (Supplementary Fig. 8b). Although the yield and selectivity of CH₃OH improved compared to CO₂R, the CH₃OH production on CoPc/CNT(I) remained inferior to that on CoPc/CNT(III) (see detailed comparison in Fig. 4a). These findings suggest that, in addition to CO enrichment, other factors may also contribute to the enhanced CH₃OH production within the CNT interior.

To further investigate these factors, we employed X-ray absorption spectroscopy (XAS) to examine the electronic structure and coordination environment of Co after CoPc encapsulation. Fourier-transformed extended X-ray absorption fine structure (FT-EXAFS) analysis confirmed that the coordination shells of Co remained unchanged compared to those in pristine CoPc molecules (Supplementary Fig. 9), indicating that CoPc retained its isolated configuration upon encapsulation. The X-ray absorption near-edge structure (XANES) spectra in Fig. 4b demonstrated that CoPc adsorbed on CNTs(I–V) exhibited identical edge positions between those of Co(II)O and Co(III)(NH₃)₆Cl₃, suggesting that the oxidation state of Co was not a determining factor for CH₃OH selectivity. Notably, CoPc/CNT(I) exhibited the strongest 1s→4p_z transition at -7716 eV, while this transition was suppressed in CoPc/CNTs(II–V) under confinement (see Fig. 4b inset and Fig. 4c). The weakened 1s→4p_z transition indicates a reduction in the D_{4h} planar symmetry of CoPc molecules, suggesting that CoPc undergoes substantial structural deformation when confined within CNTs. Furthermore, a systematic trend was observed: as the ID of CNTs increased, the intensity of the 1s→4p_z transition gradually recovered, implying a weakening of CoPc deformation due to diminishing nanoconfinement effects.

DFT calculations were performed to simulate the molecular structure of CoPc adsorbed on CNTs with varying diameters. Models were constructed for CoPc adsorbed externally on CNTs with an OD of 3 nm (CoPc-out/CNT) and internally on CNTs with ID ranging from 3 to 40 nm (CoPc-in/CNTs) to represent CoPc/CNT(I) and CoPc/

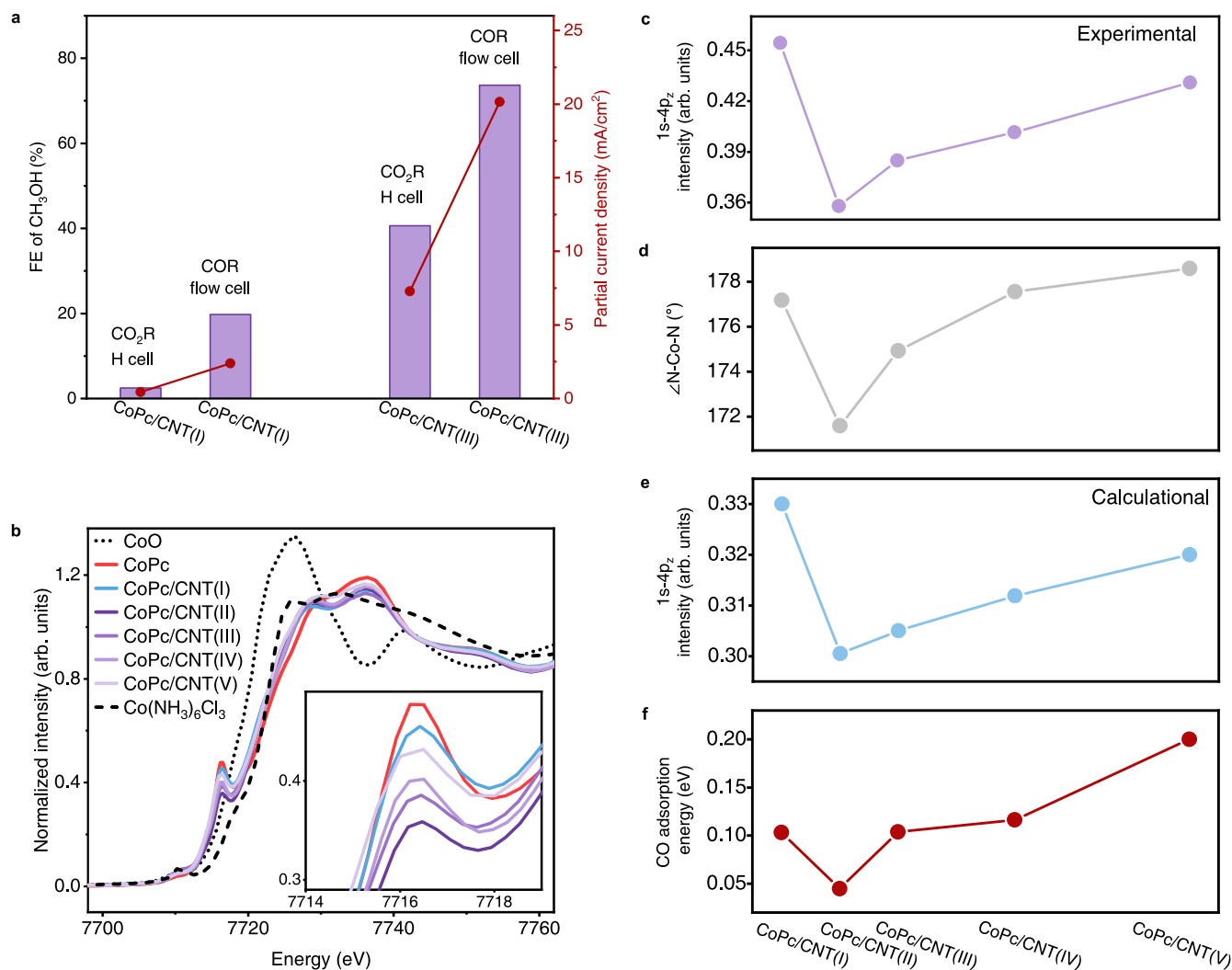


Fig. 4 | CO enrichment and CoPc deformation under nanoconfinement.

a Comparison of FE and partial current density for CH₃OH in CO₂R and COR on CoPc/CNT(I) and CoPc/CNT(III), respectively. **b** XANES spectra of CoPc/CNTs(I-V) and pristine CoPc at the Co K-edge; CoO and Co(NH₃)₆Cl₃ are shown as reference

compounds. **c** Intensity of the 1s→4p_z transition at the Co K-edge in CoPc/CNTs(I-V). **d-f** ∠N-Co-N angle in CoPc (**d**), simulated 1s→4p_z transition at the Co K-edge based on FDMNES calculations (**e**), and calculated *CO adsorption energy (**f**) in CoPc/CNTs(I-V).

CNTs(II-V), respectively (see Supplementary Fig. 10). To quantify the deformation, we used the angle between two opposite Co-N bonds (denoted as ∠N-Co-N) as a structural descriptor. In an ideal planar configuration, ∠N-Co-N is 180°. Within the CNT interior, a smaller ID resulted in stronger CoPc deformation, leading to a reduced ∠N-Co-N. For instance, as shown in Fig. 4d, ∠N-Co-N decreased from 178.6° to 171.6° as the CNT ID decreased from 40 to 3 nm. Additionally, CoPc adsorbed externally exhibited less deformation than when enclosed inside the CNT, e.g., the ∠N-Co-N of CoPc adsorbed on the outer surface of CNT(OD 3 nm) was measured to be 177.2°, while that of CoPc encapsulated within CNT(ID 3 nm) was reduced to 171.6°. These results theoretically support the structural distortion of CoPc induced by nanoconfinement.

In addition to structural deformation, we further evaluated the adsorption free energy (ΔG_{ads}) of CoPc on the inner walls of CNTs with diameters of 1.5, 2, 3, 5, 10, and 20 nm. As shown in Supplementary Fig. 11, the adsorption free energies of CoPc range from +0.64 to +1.58 eV, with the smallest CNT (d=1.5 nm) exhibiting the lowest value (+0.64 eV), primarily due to steric repulsion between the CoPc molecule and the highly curved CNT surface. When the CNT diameter exceeds 5 nm, the adsorption free energy approaches -1.6 eV, which ensures the stable

adsorption of CoPc. These findings confirm that CNTs with diameters above 5 nm are capable of stably adsorbing CoPc. Notably, we observed an inverse correlation between CoPc deformation and adsorption energy as a function of CNT diameter, suggesting that steric repulsion, rather than π - π stacking, plays a dominant role in molecular distortion. In contrast, the previous study⁴¹ demonstrated that CoPc deformation and adsorption energy exhibit consistent trends on the external CNT surfaces, where π - π stacking dominates the interaction. These findings underscore the distinct interaction mechanisms between CoPc and the inner versus outer CNT surfaces, emphasizing the unique confinement effects within CNT channels.

To further validate these findings, we employed the finite difference method for near-edge structure (FDMNES) calculations^{42,43} to simulate the theoretical XANES at the Co K-edge, which accurately reproduced our experimental spectra (Supplementary Fig. 12). The calculated intensity of the 1s→4p_z transition for CoPc/CNTs(I-V) exhibited a similar trend to that observed experimentally (Fig. 4e), confirming the validity of our DFT models. Notably, we found that structural deformation modulated the adsorption energy of *CO on Co sites. As shown in Fig. 4f, stronger deformation (smaller ∠N-Co-N) led to enhanced *CO adsorption. Taken together, these findings

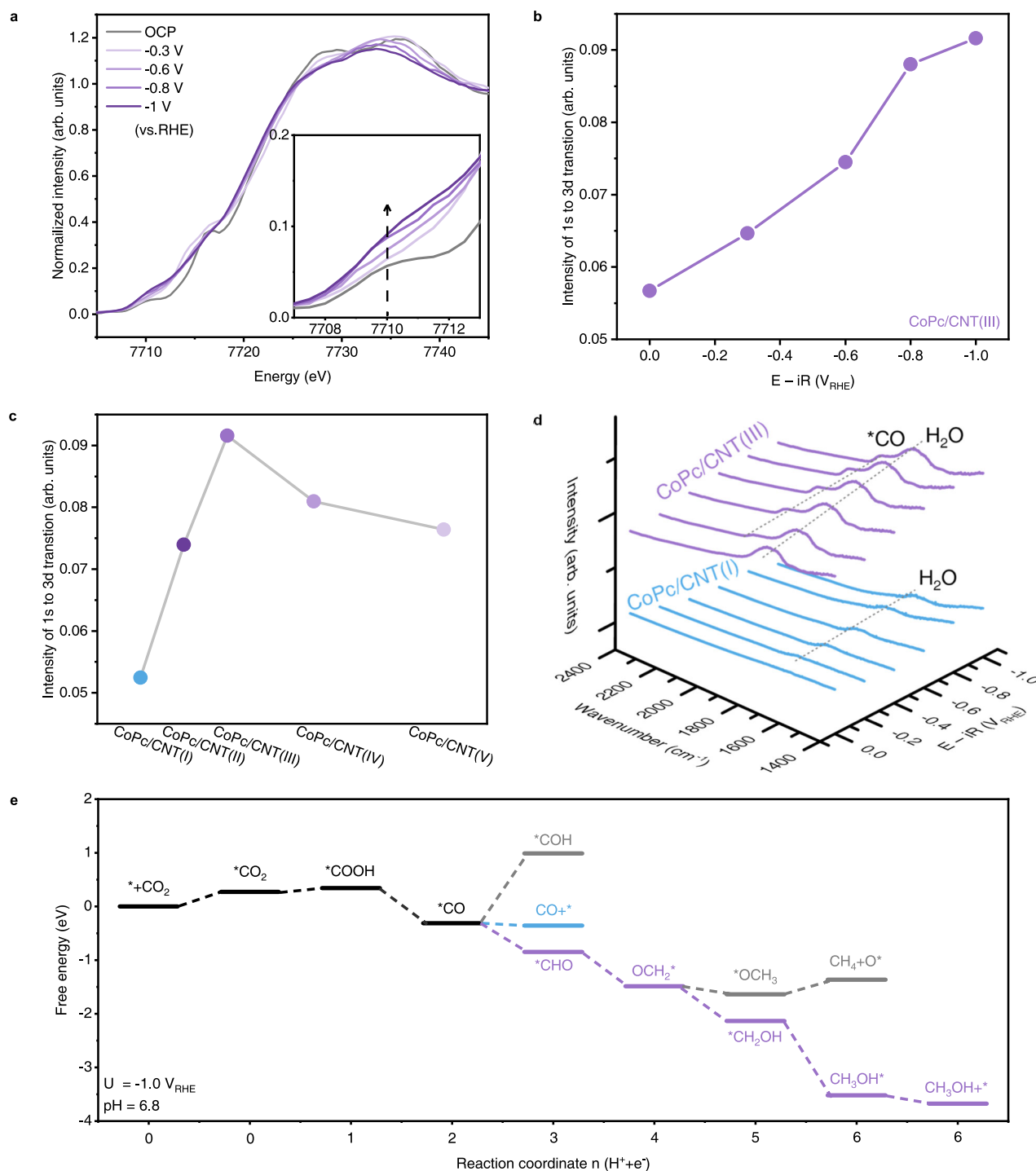


Fig. 5 | Mechanistic insights into CH_3OH production. **a** Operando Co K-edge XANES spectra of CoPc/CNT(III) under different applied potentials. **b** Variation in 1s to 3d transition intensity of CoPc/CNTs(III) under different applied potentials. **c** Comparative analysis of the 1s to 3d transition intensity in CoPc/CNTs(I-V) at -1.0

V_{RHE} . **d** Operando ATR-SEIRAS spectra of CoPc/CNT(I) and CoPc/CNT(III) recorded under various applied potentials. **e** Free energy profiles for CO_2R to CO, CH_4 , and CH_3OH on CoPc-in/CNT(3 nm).

demonstrate that encapsulating CoPc within CNTs simultaneously enriches CO and induces structural deformation, collectively altering *CO adsorption energetics and thereby promoting CH_3OH production.

Mechanistic understanding toward CH_3OH production

To monitor the process of CO_2 electrolysis, operando XAS was conducted. Figure 5a and Supplementary Fig. 13 present the operando XANES spectra of CoPc/CNTs(I-V), where minimal shifts in the absorption edge were observed across different applied potentials,

indicating that the oxidation state of Co remained largely unchanged. However, the intensity of the 1s to 3d transition (-7110 eV) in the pre-edge region exhibited significant variation under different applied potentials (Fig. 5b). Under a negative potential, the adsorption of *CO on Co led to a pronounced enhancement in the 1s to 3d transition due to the formation of back-donating π bonds between *CO and Co^{4+} . The effect of *CO binding on the pre-edge features of CoPc was further corroborated by FDMNES calculations, as illustrated in Supplementary Fig. 14.

To compare the *CO adsorption on CoPc/CNTs(I-V), we quantified the intensity of the $1s \rightarrow 3d$ transition as an indicator of *CO coverage on CoPc. Notably, CoPc/CNT(III) exhibited a marked increase in $1s \rightarrow 3d$ intensity under negative potential, whereas CoPc/CNT(I) displayed negligible changes (Supplementary Fig. 13). Thus, it is reasonable to infer that a greater number of *CO intermediates were adsorbed on CoPc/CNT(III), indicating its enhanced *CO adsorption capability. Further comparison of the $1s \rightarrow 3d$ intensity across CoPc/CNTs(I-V) at $-1.0 V_{RHE}$ (Fig. 5c) revealed that all CoPc/CNTs(II-V) exhibited a stronger $1s \rightarrow 3d$ transition than CoPc/CNT(I), confirming that nanoconfinement significantly enhances *CO adsorption on catalytic Co centers. To directly track *CO adsorption, we performed operando attenuated total reflection surface-enhanced infrared absorption spectroscopy (ATR-SEIRAS). For CoPc/CNT(III), a *CO signal at -1920 cm^{-1} was detected below $-0.2 V_{RHE}$. In contrast, no *CO signal was observed on CoPc/CNT(I) across the entire potential range (Fig. 5d), indicating weak *CO adsorption on CoPc/CNT(I), consistent with our operando XANES findings. To gain mechanistic insights into the CO_2 -to- CH_3OH conversion, we examined the energy profiles of CO_2 electrolysis on CoPc-in/CNT (ID 3 nm), as depicted in Fig. 5e. The most favorable CH_3OH formation pathway was identified as $^*CO_2 \rightarrow ^*COOH \rightarrow ^*CO \rightarrow ^*CHO \rightarrow ^*CH_2O \rightarrow ^*CH_2OH \rightarrow ^*CH_3OH \rightarrow ^* + CH_3OH$, based on DFT calculations. Under $U = -1.0 V_{RHE}$ and $pH = 6.8$, *CO preferentially underwent further reduction rather than desorbing as CO. Notably, a more negative potential further facilitates the reduction of *CO rather than its desorption to $CO(g)$ (Supplementary Fig. 15). Consequently, the onset potential for CH_3OH production was more negative than that for CO in the experiments. Additionally, the formation pathway of CH_4 from *CO was studied, which proceeded through the sequence $^*CO \rightarrow ^*CHO \rightarrow ^*CH_2O \rightarrow ^*OCH_3 \rightarrow ^*O + CH_4$. The cleavage of the C-O bond in *OCH_3 was found to be energetically demanding, thereby increasing the energy barrier for CH_4 formation and resulting in its lower selectivity compared to CH_3OH .

On the other hand, the hydrogen evolution reaction (HER) is the primary competing pathway that may reduce the efficiency of CO_2R . To further elucidate this issue, we performed free energy calculations for HER and compared them with those of CO_2R (Supplementary Fig. 16). Our results indicate that the free energy changes of the potential-determining steps (PDS) for both CO_2R and HER are nearly identical, suggesting a strong competition between the two pathways. Furthermore, we compared the adsorption energies of *CO_2 and *H at various potentials and observed that *H adsorption becomes more favorable than *CO_2 adsorption as the potential becomes more negative (Supplementary Fig. 17). This trend is consistent with our experimental observations: the FE of HER is only 4% at $-0.83 V_{RHE}$, but increases to 55% at $-0.98 V_{RHE}$. We believe that HER competition could be effectively mitigated in future studies through modulation of the interfacial environment and optimization of reactor configuration.

Discussion

In this work, we demonstrated that the inner cavity of CNTs can serve as a nanoreactor to facilitate the electrochemical reduction of CO_2 to CH_3OH by CoPc. The steric confinement restricted the outward diffusion of CO and suppressed the free desorption of *CO from Co catalytic sites. More importantly, the encapsulated CoPc molecules experienced more pronounced structural deformation, resulting in enhanced *CO adsorption. Both effects synergistically promoted the deep reduction of *CO , thereby enhancing CH_3OH production. By tuning the ID of CNTs, we achieved a maximum CH_3OH selectivity of 41%, with CH_3OH being the sole liquid product. Overall, we explicitly apply the concept of nanoconfinement to rationalize the unique CH_3OH selectivity observed in CoPc/CNTs. This study offers insights into the mechanistic understanding of CO_2 -to- CH_3OH conversion and

enhances our comprehension of how confined environments influence catalytic pathways and product selectivity.

Methods

Synthesis of CoPc/CNTs(I-V)

All CNTs were pretreated by calcination and acid washing before use. Specifically, the CNTs were calcined at $400\text{ }^\circ\text{C}$ in air for 5 h to remove amorphous carbon. After annealing, the CNTs were thoroughly washed with 10 wt% HCl aqueous solution and deionized water to eliminate metal impurities. CoPc/CNTs were synthesized by dissolving 2 mg of CoPc in 30 mL of DMF, followed by dispersing 30 mg of purified CNTs in the CoPc/DMF solution. The mixture was sonicated for 30 min and stirred for 48 h to facilitate the infiltration of the solution into CNTs. Subsequently, the sample was centrifuged and thoroughly washed with DMF, ethanol, and deionized water. Finally, the CoPc/CNTs powder was obtained after lyophilization.

Synthesis of CoPc/CNT(III) via mild stirring

Initially, 2 mg of CoPc was dissolved in 30 mL of DMF, followed by the addition of 30 mg of purified CNT(III). The mixture was gently stirred for 30 min at room temperature. After stirring, the sample was centrifuged and thoroughly washed with DMF, ethanol, and deionized water. The final product was obtained after lyophilization.

Synthesis of CoPc/CNT(III) using ethanol as solvent

Initially, 2 mg of CoPc was dissolved in 30 mL of ethanol, followed by the addition of 30 mg of purified CNT(III). The mixture was sonicated for 30 min and stirred for 48 h. Subsequently, the sample was centrifuged and thoroughly washed with DMF, ethanol, and deionized water. Finally, the powder was obtained after lyophilization.

TEM characterization

The CoPc/CNTs samples were dispersed in ethanol and drop-casted onto a TEM copper grid. HR-TEM and STEM imaging were performed using a spherical aberration-corrected transmission electron microscope (GrandARM300F, Japan) operated at an accelerating voltage of 80 kV at room temperature. HR-TEM images were acquired with an exposure time of 1.0 s using a Gatan Oneview IS Camera. The vacuum level in the sample chamber was maintained at -5×10^{-6} Pa. Simulated TEM images were generated using the multislice program QSTEM, with the spherical-aberration coefficient (Cs) set to $2.7\text{ }\mu\text{m}$ and defocus set to -15 nm based on experimental calibration. The electron beam dose for simulations was $5 \times 10^6\text{ e/nm}^2$.

Working electrode preparation

The catalyst ink was prepared by dispersing 2 mg of CoPc/CNTs and $6\text{ }\mu\text{L}$ of 5 wt % Nafion in 2 mL of ethanol. The ink was sonicated for at least 1 h to achieve thorough dispersion. For CO_2R measurements in the H-cell, 200 μL of the catalyst ink was drop-casted onto a carbon paper (Toray O30) with a geometric area of 0.5 cm^2 and dried overnight at room temperature. For electrochemical measurements in the flow cell, 400 μL of the catalyst ink was drop-casted onto a gas diffusion layer (YLS 30 T) with a geometric area of 1 cm^2 and dried overnight at room temperature. The mass loading of CoPc/CNTs is $\sim 0.4\text{ mg/cm}_{\text{geo}}^2$.

Electrochemical measurements

The catalytic performance was evaluated in a customized H-cell, where the two compartments were separated by a Nafion 117 proton exchange membrane. The Nafion membrane underwent an immersion treatment in a 5% hydrogen peroxide solution at $80\text{ }^\circ\text{C}$ for an hour, followed by rinsing in deionized water for 30 min, then treatment in 5% sulfuric acid (by mass) at $80\text{ }^\circ\text{C}$ for another hour, and a final deionized water rinse for 30 min. Each compartment contained 10 mL of 0.1 M $KHCO_3$ aqueous

electrolyte, and the working electrode compartment was designed to be gas-tight for precise quantification of gaseous products. The electrolyte was saturated with CO₂ by purging at a flow rate of 5 sccm for 30 min before and during each measurement. No special storage conditions were needed for the electrolyte beyond room temperature. Ag/AgCl (3.5 M KCl, Gaoss Union, Inc.) and Pt mesh were employed as the reference and counter electrodes, respectively. All electrochemical measurements were performed at room temperature (23 ± 2 °C) using a Gamry Interface 3000 potentiostat. The flow rate verification was conducted using a bubble flowmeter at the cathode chamber's outlet. All reported potentials were converted to the RHE scale with 100% resistance compensation, using the following formula:

$$E_{vs.RHE} = E_{vs.Ag/AgCl} + 0.205 V + 0.0591 \times \text{pH} - i \times R \quad (1)$$

where pH represents the electrolyte pH, -6.8 ± 0.1 in 0.1 M CO₂-saturated KHCO₃ solution. The potential of the Ag/AgCl reference electrode was calibrated against a reversible hydrogen electrode (RHE, Gaoss Union, Inc.). Potentials include a full iR compensation, with the uncompensated resistance (*R_Ω*) determined by extrapolating high-frequency impedance data, averaging around 10 ± 2 Ω in 0.1 M KHCO₃. The non-iR corrected voltammograms for CoPc/CNTs(l-v) was shown in the Supplementary Fig. 18.

For CO₂R and COR measurements in the customized flow cell, a GDE-supported catalyst was used as the working electrode, while Ag/AgCl and Ni foam served as the reference and counter electrodes, respectively. A Nafion N117 membrane was used to separate the anodic and cathodic compartments. CO₂ or CO gas (flow rate, 20 sccm) was continuously supplied to the cathodic electrolyte, while a 0.5 M KHCO₃ electrolyte (10 mL min⁻¹) was circulated in both compartments using a peristaltic pump.

Product quantification

The gaseous products were analyzed using an online GC (Agilent 7890B) equipped with a thermal conductivity detector (TCD) and a flame ionization detector (FID). Liquid products were quantified using a 400 MHz NMR spectrometer (AVANCE III HD) with dimethyl sulfide (DMSO) as the internal standard. The solvent pre-saturation technique was implemented to suppress the water peak⁴⁵. The Faradaic efficiency and production rate were calculated according to the following equations:

Calculation of the Faradaic efficiency of gas products:

$$\text{FE}(\text{gas}) = \frac{F_{\text{flow}} \times \left(\frac{C_{\text{gas}}}{V_m}\right) \times n \times F}{I_{\text{total}} \times 60} \times 100 \quad (2)$$

Calculation of the Faradaic efficiency of liquid products:

$$\text{FE}(\text{liquid}) = \frac{C_{\text{liquid}} \times V \times n \times F}{Q_{\text{total}}} \times 100 \quad (3)$$

where:

FE (gas): Faradaic efficiency of the gas product (%)

FE (liquid): Faradaic efficiency of the liquid product (%)

F_{flow}: flow rate of CO₂ (mL min⁻¹)

C_{gas}: volume fraction of gas product determined by online GC

V_m: molar volume of an ideal gas (24.5 mL mol⁻¹ at NTP)

C_{liquid}: concentration of liquid product after electrolysis, determined by NMR (mol L⁻¹)

V: volume of electrolyte in the working compartment (L)

I_{total}: steady-state cell current (A)

Q_{total}: total charge passed during 1 h of electrolysis (C)

n: number of electrons transferred per product molecule

F: Faradaic constant (96,485 C mol⁻¹)

Operando XAS measurement

Experiments were conducted at the BL11B beamline of the Shanghai Synchrotron Radiation Facility (SSRF). A monochromatized X-ray beam was generated using a double-crystal Si(111) monochromator, and the photon energy was calibrated to the first inflection point of the Co K-edge (7709 eV) using a Co foil reference. All spectra were collected in fluorescence mode using a Lytle detector filled with argon gas. The acquired spectra were normalized and analyzed using the ATHENA software package.

Operando XAS measurements were performed using a custom-designed three-electrode H-cell (Supplementary Fig. 19). The working electrode was prepared by depositing CoPc/CNTs onto carbon paper at a loading of -2 mg/cm². A Pt wire and an Ag/AgCl electrode were used as the counter and reference electrodes, respectively. A 0.1 M KHCO₃ electrolyte was used, with continuous CO₂ bubbling throughout the measurements.

FDMNES calculation

Co K-edge XANES simulations were performed using the FDMNES software, which employs the Finite Difference Method (FDM) and the Green's formalism (multiple scattering) on a muffin-tin potential^{42,43}. The structural models of CoPc/CNTs were generated and optimized using DFT calculations. The radius used in the XANES simulations was set to 6.5 Å.

Operando ATR-SEIRAS experiments

Operando ATR-SEIRAS experiments were conducted using a customized spectroelectrochemical cell on a Nicolet 6700 spectrometer, equipped with a liquid nitrogen-cooled mercury cadmium telluride (MCT) detector and an attenuated total reflection (ATR) accessory. A thin Au film was chemically deposited onto the surface of a silicon prism. Subsequently, the catalyst ink was drop-casted onto the pre-deposited Au film and air-dried to prepare the working electrode. An Ag/AgCl electrode was used as the reference electrode, and a graphite rod served as the counter electrode. The electrolyte was 0.1 M KHCO₃ with continuous CO₂ bubbling. All electrochemical tests were controlled using a Gamry Interface 1010 potentiostat. All spectra were recorded in absorbance units at a resolution of 4 cm⁻¹, with 64 scans per spectrum.

Computational methodology

A hybrid Quantum Mechanics/Machine Learning (QM/ML) method⁴⁶ was employed to simulate CoPc/CNTs with diameters ranging from 3 nm to 40 nm. In the QM/ML approach, the CoPc/CNTs system was divided into three regions: inner, boundary, and outer. The inner region comprised the CoPc active site and partial CNT substrate atoms interacting with CoPc, while the outer region contained atoms distant from the active site. The boundary region was located between the inner and outer regions, as illustrated in Supplementary Fig. 20. The inner and boundary regions were treated with quantum mechanics (QM), while the outer and boundary regions were modeled using machine-learning (ML) potentials. Hydrogen atoms were employed as link atoms to cap unsaturated carbon atoms in both the QM and ML regions. Constrained optimization was subsequently conducted using Lagrange multipliers, which enforced the overlap of atomic coordinates in the boundary regions of both QM and ML domains. More details on the computational methodology can be found in Supplementary Information and our previous work⁴⁶. The atomic coordinates of the optimized computational models were provided as Supplementary Data 1.

For the ML region, a global neural network (G-NN) potential developed by our group was employed⁴⁷. The G-NN potential follows the Behler-Parrinello NN framework with atoms as the objects for energy resolution and summation, where the input layer utilizes the power-type structure descriptor (PTSD). The G-NN potential was

generated by iteratively fitting the global PES data obtained from DFT via stochastic surface walking (SSW) global structural search. The root-mean-square errors (RMSE) of the final G-NN potential for energy and force were 7.379 meV/atom and 0.269 eV/Å, respectively.

For the QM Region, spin-polarized DFT calculations were performed using the Vienna ab initio Simulation Package (VASP), employing the generalized gradient approximation (GGA) with the Perdew-Burke-Ernzerhof (PBE) functional for exchange correlation. An energy cutoff of 400 eV was used for all calculations, and a Γ -only k-point mesh was utilized for Brillouin zone integration. The atomic positions were optimized until the residual force was below 0.08 eV Å⁻¹. The energy convergence criterion was set to 10⁻⁵ eV. To account for the electronic correlation of Co 3d electrons, a rotationally invariant DFT + U approach with U - J = 3.3 eV was applied. We tested U - J values of 3.0, 3.3, and 3.5 eV, which show that the choice of the Hubbard U-J parameter would not significantly affect our conclusions. More details are given in Supplementary Method 2.

The computational hydrogen electrode (CHE) method was used to compute the free energy diagrams for the electrocatalytic CO₂R process. The core principle of the CHE method is to establish equilibrium between the electron-proton pair (H⁺ + e⁻) and molecular H₂ at the standard hydrogen electrode. The free energy change of each elementary step (ΔG_i) in CO₂R is then calculated using Eq. (4) at an electrode potential of U = 1.0 V (vs. RHE).

$$\Delta G_i = \Delta E_i + \Delta E_{\text{ZPE}} + \Delta H_{\text{O} \rightarrow 298.15\text{K}} - T\Delta S - eU + \Delta G_{\text{pH}} \quad (4)$$

where ΔE_i represents the electronic energy difference obtained directly from QM/ML calculations. ΔE_{ZPE} , $\Delta H_{\text{O} \rightarrow 298.15\text{K}}$, and $T\Delta S$ correspond to corrections for zero-point energy, enthalpy, and entropy, respectively, which are determined using vaspkit⁴⁸. The term ΔG_{pH} accounts for the free energy correction due to pH, following the Nernst equation ($\Delta G_{\text{pH}} = -k_{\text{B}}T \ln(10) \times \text{pH}$). The numerical values of each term are provided in Supplementary Table 3.

Data availability

The data supporting the findings of this study are available within the Article and its Supplementary Information files. The raw data files in another format are available from the corresponding authors upon reasonable request. Source data are provided with this paper.

References

- Xiao, J., Pan, X., Guo, S., Ren, P. & Bao, X. Toward fundamentals of confined catalysis in carbon nanotubes. *J. Am. Chem. Soc.* **137**, 477–482 (2015).
- Dong, B. et al. Deciphering nanoconfinement effects on molecular orientation and reaction intermediate by single molecule imaging. *Nat. Commun.* **10**, 4815 (2019).
- Grommet, A. B., Feller, M. & Klajn, R. Chemical reactivity under nanoconfinement. *Nat. Nanotechnol.* **15**, 256–271 (2020).
- Pan, X. et al. Enhanced ethanol production inside carbon-nanotube reactors containing catalytic particles. *Nat. Mater.* **6**, 507–511 (2007).
- Jiao, F. et al. Selective conversion of syngas to light olefins. *Science* **351**, 1065–1068 (2016).
- Riscoe, A. R. et al. Transition state and product diffusion control by polymer–nanocrystal hybrid catalysts. *Nat. Catal.* **2**, 852–863 (2019).
- Eads, C. N. et al. Enhanced catalysis under 2D silica: A CO oxidation study. *Angew. Chem. Int. Ed.* **60**, 10888–10894 (2021).
- Hu, Z. P. et al. Atomic insight into the local structure and micro-environment of isolated Co-motifs in MFI zeolite frameworks for propane dehydrogenation. *J. Am. Chem. Soc.* **144**, 12127–12137 (2022).
- Ma, Y. et al. Germanium-enriched double-four-membered-ring units inducing zeolite-confined subnanometric Pt clusters for efficient propane dehydrogenation. *Nat. Catal.* **6**, 506–518 (2023).
- Zhou, H. et al. Organocatalytic stereoselective cyanosilylation of small ketones. *Nature* **605**, 84–89 (2022).
- Zhuang, T. T. et al. Copper nanocavities confine intermediates for efficient electrosynthesis of C₃ alcohol fuels from carbon monoxide. *Nat. Catal.* **1**, 946–951 (2018).
- O'Mara, P. B. et al. Cascade reactions in nanozymes: Spatially separated active sites inside Ag-core-porous-Cu-shell nanoparticles for multistep carbon dioxide reduction to higher organic molecules. *J. Am. Chem. Soc.* **141**, 14093–14097 (2019).
- Yang, P. P. et al. Protecting copper oxidation state via intermediate confinement for selective CO₂ electroreduction to C₂₊ fuels. *J. Am. Chem. Soc.* **142**, 6400–6408 (2020).
- Kim, J. Y. et al. Quasi-graphitic carbon shell-induced Cu confinement promotes electrocatalytic CO₂ reduction toward C₂₊ products. *Nat. Commun.* **12**, 3765 (2021).
- Liu, C. et al. Nanoconfinement engineering over hollow multi-shell structured copper towards efficient electrocatalytic C–C coupling. *Angew. Chem. Int. Ed.* **61**, e202113498 (2022).
- Birdja, Y. Y. et al. Advances and challenges in understanding the electrocatalytic conversion of carbon dioxide to fuels. *Nat. Energy* **4**, 732–745 (2019).
- Peterson, A. A., Abild-Pedersen, F., Studt, F., Rossmeisl, J. & Nørskov, J. K. How copper catalyzes the electroreduction of carbon dioxide into hydrocarbon fuels. *Energy Environ. Sci.* **3**, 1311–1315 (2010).
- Nitopi, S. et al. Progress and perspectives of electrochemical CO₂ reduction on copper in aqueous electrolyte. *Chem. Rev.* **119**, 7610–7672 (2019).
- Ross, M. B. et al. Designing materials for electrochemical carbon dioxide recycling. *Nat. Catal.* **2**, 648–658 (2019).
- Wagner, A., Sahn, C. D. & Reisner, E. Towards molecular understanding of local chemical environment effects in electro- and photocatalytic CO₂ reduction. *Nat. Catal.* **3**, 775–786 (2020).
- Vijay, S. et al. Unified mechanistic understanding of CO₂ reduction to CO on transition metal and single atom catalysts. *Nat. Catal.* **4**, 1024–1031 (2021).
- Chang, Q. et al. Metal-coordinated phthalocyanines as platform molecules for understanding isolated metal sites in the electrochemical reduction of CO₂. *J. Am. Chem. Soc.* **144**, 16131–16138 (2022).
- Yang, H. B. et al. Atomically dispersed Ni(I) as the active site for electrochemical CO₂ reduction. *Nat. Energy* **3**, 140–147 (2018).
- Gu, J., Hsu, C. S., Bai, L., Chen, H. M. & Hu, X. Atomically dispersed Fe³⁺ sites catalyze efficient CO₂ electroreduction to CO. *Science* **364**, 1091–1094 (2019).
- Ren, S. et al. Molecular electrocatalysts can mediate fast, selective CO₂ reduction in a flow cell. *Science* **365**, 367–369 (2019).
- Gu, H. et al. Graphdiyne/graphene heterostructure: A universal 2D scaffold anchoring monodispersed transition-metal phthalocyanines for selective and durable CO₂ electroreduction. *J. Am. Chem. Soc.* **143**, 8679–8688 (2021).
- Wu, Y., Jiang, Z., Lu, X., Liang, Y. & Wang, H. Domino electroreduction of CO₂ to methanol on a molecular catalyst. *Nature* **575**, 639–642 (2019).
- Boutin, E. et al. Aqueous electrochemical reduction of carbon dioxide and carbon monoxide into methanol with cobalt phthalocyanine. *Angew. Chem. Int. Ed.* **58**, 16172–16176 (2019).
- Ren, X. et al. In-situ spectroscopic probe of the intrinsic structure feature of single-atom center in electrochemical CO/CO₂ reduction to methanol. *Nat. Commun.* **14**, 3401 (2023).

30. Su, J. et al. Strain enhances the activity of molecular electrocatalysts via carbon nanotube supports. *Nat. Catal.* **6**, 818–828 (2023).
31. Rooney, C. et al. Active sites of cobalt phthalocyanine in electrocatalytic CO₂ reduction to methanol. *Angew. Chem. Int. Ed.* **63**, e202310623 (2024).
32. Yao, L., Rivera-Cruz, K. E., Zimmerman, P. M., Singh, N. & McCrory, C. C. L. Electrochemical CO₂ reduction to methanol by cobalt phthalocyanine: Quantifying CO₂ and CO binding strengths and their influence on methanol production. *ACS Catal.* **14**, 366–372 (2024).
33. Smith, B. W., Monthioux, M. & Luzzi, D. E. Encapsulated C₆₀ in carbon nanotubes. *Nature* **396**, 323–324 (1998).
34. Li, L. J., Khlobystov, A. N., Wiltshire, J. G., Briggs, G. A. D. & Nicholas, R. J. Diameter-selective encapsulation of metallocenes in single-walled carbon nanotubes. *Nat. Mater.* **4**, 481–485 (2005).
35. Schulte, K. et al. Assembly of cobalt phthalocyanine stacks inside carbon nanotubes. *Adv. Mater.* **19**, 3312–3316 (2007).
36. Pan, X. & Bao, X. The effects of confinement inside carbon nanotubes on catalysis. *Acc. Chem. Res.* **44**, 553–562 (2011).
37. Botos, A. et al. Carbon nanotubes as electrically active nanoreactors for multi-step inorganic synthesis: Sequential transformations of molecules to nanoclusters and nanoclusters to nanoribbons. *J. Am. Chem. Soc.* **138**, 8175–8183 (2016).
38. Yang, X. et al. Host-guest molecular interaction enabled separation of large-diameter semiconducting single-walled carbon nanotubes. *J. Am. Chem. Soc.* **143**, 10120–10130 (2021).
39. Ebbesen, T. W. Wetting, filling and decorating carbon nanotubes. *J. Phys. Chem. Solids* **57**, 951–955 (1996).
40. Ghani, F., Kristen, J. & Riegler, H. Solubility Properties of Unsubstituted Metal Phthalocyanines in Different Types of Solvents. *J. Chem. Eng. Data* **57**, 439–449 (2012).
41. Zhou, Z.-P. et al. Understanding the influence of bending on OER activity in metal phthalocyanines: A first-principles study. *Appl. Surf. Sci.* **618**, 156582 (2023).
42. Bunău, O. & Joly, Y. Self-consistent aspects of X-ray absorption calculations. *J. Phys.: Condens. Matter* **21**, 345501 (2009).
43. Guda, S. A. et al. Optimized finite difference method for the full-potential XANES simulations: Application to molecular adsorption geometries in MOFs and metal–ligand intersystem crossing transitions. *J. Chem. Theory Comput.* **11**, 4512–4521 (2015).
44. Gu, H. et al. A Two-dimensional van der waals heterostructure with isolated electron-deficient cobalt sites toward high-efficiency CO₂ electroreduction. *J. Am. Chem. Soc.* **144**, 21502–21511 (2022).
45. Giraudeau, P., Silvestre, V. & Akoka, S. Optimizing water suppression for quantitative NMR-based metabolomics: A tutorial review. *Metabolomics* **11**, 1041–1055 (2015).
46. Kang, Y., Li, Y. F. & Liu, Z. P. Unveiling curvature effect on Fe atom embedded N-doped carbon nanotubes for electrocatalytic oxygen reduction reactions using hybrid quantum-mechanics/machine-learning potential. *J. Phys. Chem. C* **128**, 3127–3135 (2024).
47. Huang, S.-D., Shang, C., Kang, P. L. & Liu, Z. P. Atomic structure of boron resolved using machine learning and global sampling. *Chem. Sci.* **9**, 8644–8655 (2018).
48. Wang, V., Xu, N., Liu, J. C., Tang, G. & Geng, W. T. VASPKIT: A user-friendly interface facilitating high-throughput computing and analysis using VASP code. *Comput. Phys. Commun.* **267**, 108033 (2021).

Acknowledgements

This work is funded by the National Key R&D Program of China (2024YFB4006800), Natural Science Foundation of China (Grants 22272029 and 22472036), Science and Technology Commission of Shanghai Municipality (Grant 22520711100, 22ZR1415700, and 23ZR1406900), the Fundamental Research Funds for the Central Universities (20720220008) and the Shanghai Rising-Star Program (21QA1406300).

Author contributions

L.Z. designed and conceived the experiment. G.S., J.Z., T.L., C.Y., M.C., Y.S., X.G., and J.W. fabricated the electrodes and performed the electrochemical characterization and/or data analysis. W.Z. and K.C. contributed to the TEM characterizations. Y.K. and Y.L. worked on the DFT calculations. G.S. and L.Z. wrote the manuscript. All authors discussed the results and commented on the paper.

Competing interests

The authors declare no competing interests.

Additional information

Supplementary information The online version contains supplementary material available at <https://doi.org/10.1038/s41467-025-62656-3>.

Correspondence and requests for materials should be addressed to Ye-Fei Li, Kecheng Cao or Liming Zhang.

Peer review information *Nature Communications* thanks Yuhang Wang, Zheng Hu, and the other, anonymous, reviewer(s) for their contribution to the peer review of this work. A peer review file is available.

Reprints and permissions information is available at <http://www.nature.com/reprints>

Publisher's note Springer Nature remains neutral with regard to jurisdictional claims in published maps and institutional affiliations.

Open Access This article is licensed under a Creative Commons Attribution-NonCommercial-NoDerivatives 4.0 International License, which permits any non-commercial use, sharing, distribution and reproduction in any medium or format, as long as you give appropriate credit to the original author(s) and the source, provide a link to the Creative Commons licence, and indicate if you modified the licensed material. You do not have permission under this licence to share adapted material derived from this article or parts of it. The images or other third party material in this article are included in the article's Creative Commons licence, unless indicated otherwise in a credit line to the material. If material is not included in the article's Creative Commons licence and your intended use is not permitted by statutory regulation or exceeds the permitted use, you will need to obtain permission directly from the copyright holder. To view a copy of this licence, visit <http://creativecommons.org/licenses/by-nc-nd/4.0/>.

© The Author(s) 2025